Hindawi
International Journal of Antennas and Propagation
Volume 2023, Article ID 5545085, 16 pages
https://doi.org/10.1155/2023/5545085

Research Article

Design of a Three-Dimensional Uniform UHF Near-Field RFID Reader Antenna

Yuan Yao,[1] **Yani Xue**,[1] **Xiaojuan Ren**,[1] **Junsheng Yu**,[1] **Xiaohe Cheng**,[1] **and Xiaodong Chen**[2]

[1]*School of Electronic Engineering, Beijing University of Posts and Telecommunications, Beijing 100876, China*
[2]*School of Engineering and Computer Science, Queen Mary University of London, Mile End Road, London E1 4NS, UK*

Correspondence should be addressed to Yuan Yao; yaoy@bupt.edu.cn

Received 21 April 2023; Revised 22 August 2023; Accepted 11 November 2023; Published 24 November 2023

Academic Editor: Trushit Upadhyaya

This paper proposes a three-dimensional uniform ultra-high frequency (UHF) near-field radio frequency identification (RFID) reader antenna. The antenna achieves a uniform electric field in the x and y directions by placing a single branch microstrip line along the x-axis and y-axis directions, respectively. It reaches a uniform electric field in the z-direction by a centrosymmetric four-branch microstrip line. The proposed antenna achieves three-dimensional direction uniformity through a reconfigurable method. The impedance matching bandwidth range of S_{11} <−10 dB for simulation and measurement includes 0.66 to 0.98 GHz, which can meet the near-field RFID operation frequency band demand. The isolation degrees between ports are less than −24.6 dB within the UHF RFID frequency band (0.86 to 0.96 GHz). In addition, the antenna also has the characteristic of low gain in the far field, and the maximum gain in the far field is less than −27 dBi when operating at different ports. The test results show that the proposed antenna three-dimensional uniform volume of dipole tags above the antenna is 99 mm × 99 mm × 20 mm, and the reading volume of the near-field tags is 40 mm × 40 mm × 5 mm. When the tags are placed on a book, there will be a slight variation in the reading range of the tags.

1. Introduction

Recently, ultrahigh-frequency (UHF) radio frequency identification (RFID) technology has been widely concerned because of its rapid identification characteristics. Also, it has moved from obscurity into mainstream applications that help speed the handling of manufactured goods and materials. It is a well-known wireless application in traceability, logistics, and access control [1–3].

UHF RFID systems are divided into near-field and far-field systems according to the different recognition distances. Near-field systems are generally used for recognition distances less than one meter. In recent years, near-field application scenarios like bright bookshelves and intelligent vending machines have become more and more extensive [4–6]. The performance of the near-field application system mainly depends on the near-field reader antenna [4, 7–9]. Hence, designing a reliable UHF RFID near-field reader antenna is worthwhile.

According to the different coupling methods, the near-field RFID reader antenna is divided into a magnetic and an electrically coupled antenna. Magnetic coupling antenna communicates with magnetic tags through alternating magnetic fields in the near-field region. Shi et al. proposed a zero-phase shift circular antenna to generate a strong and uniform magnetic field [10, 11]. Yao et al. [12] realized uniform magnetic field distribution in the near-field region through two meandering open microstrip lines with reverse current. The magnetic coupling antenna can read a large number of magnetic labels through a uniform magnetic field distribution in the near-field area, but its low reading distance limits its application scenarios.

Electrically coupled antenna exploits alternating electric fields for information interactive with tags. A meander microstrip line loaded with a 50-ohm resistance antenna is designed in [13] can generate a strong and uniform E-field in the near-field region. An antenna based on the EM coupling between an open-ended MS feed line and periodic planar

metal strips was designed and applied to the smart bookshelf [14]. However, these types of antenna polarization modes are linear polarization, which restricts the placement orientation of linear polarization tags during the actual reading process. To solve this problem, Yao et al. designed a variety of multipolarized near-field antennas by introducing a 90° phase shifter between the currents flowing along the opposite side of two branches [15–17]. In addition, some circularly polarized antennas are proposed for RFID systems [18–20]. These antennas achieved the detection of linearly polarized tags in an arbitrary orientation parallel to the antenna surface. However, they are unable to accurately detect linearly polarized labels perpendicular to the antenna surface, which limits the detection of linearly polarized labels in arbitrarily three-dimensional orientation.

In this paper, we propose a near-field RFID reader antenna with low gain and uniform three-dimensional electric field components in the near-field region. The proposed antenna is composed of two mutually perpendicular single-branch microstrip lines, one centrally symmetrical four-branch microstrip line, and four rectangular patches. Through the time-sharing operation of three feeding ports, the uniformity of the three-dimensional components of the electric field is realized. The measurement results show that the −10 dB impedance bandwidth of the antenna is 0.66 to 0.98 GHz, which covers the standardized bandwidth of UHF RFID. When linearly polarized electrically coupled tags are placed arbitrarily in three-dimensional space and detected by the proposed antenna, the read volume for 100% read rate of Alien A9662 tags is 99 mm × 99 mm × 20 mm, and the reading volume for 100% read rate of the near-field tags Alien SIT is 40 mm × 40 mm × 5 mm. The proposed antenna can detect tags perpendicular to its surface, making tag detection more accurate and application scenarios more diverse.

2. Reader Antenna Design

2.1. Antenna Configuration. The proposed multiport reconfigurable antenna configuration is shown in Figure 1. It has three layers structure. The first layer is composed of two single-segment microstrip lines and a central symmetrical four-segment microstrip line, which is fabricated on an FR4 substrate with a thickness of 2 mm. The end of each microstrip branch relates to a 50 Ω load. Therefore, the surface of the microstrip line will generate a traveling wave current, which can realize the broadband of the antenna. The second layer is four parasitic patches with a thickness of 0.035 mm of metal copper, which are fabricated on an FR4 substrate with a thickness of 2.6 mm. The last layer is the grounding plate with copper material. The total thickness of the antenna structure is 4.6 mm. The antenna has three feeding ports to provide electromagnetic energy to the radiation structure. Port 1 is located in the center of a centrally symmetrical four-branch microstrip line. Port 2 is located to the right of the single branch along the x-axis direction. Port 3 is below the single-stub microstrip line along the y-axis direction. They are fed coaxially through the 50 Ω SMA connector. The optimized dimensions of the antenna are shown in Table 1.

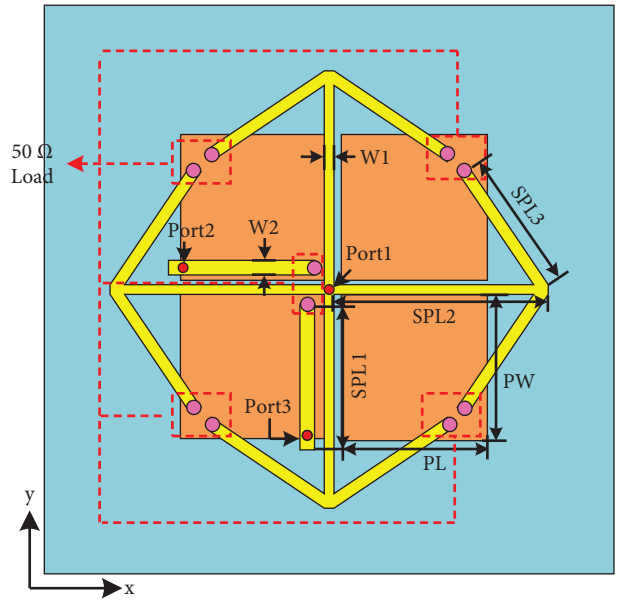

Figure 1: Configuration of the multiport reconfigurable antenna.

Table 1: Dimensions of optimized antenna design.

Parameters	Description	Value (mm)
HG	Height of the ground	0.035
HP	Height of the patches	0.035
HS1	Height of the substrate 1	2
HS2	Height of the substrate 2	2.6
HSP	Height of the microstrip line	0.035
L	Substrate length	117
W	Substrate width	117
$W1$	Microstrip line width 1	2
$W2$	Microstrip line width 2	3
SPL1	Microstrip line length 1	30
SPL2	Microstrip line length 2	44
SPL3	Microstrip line length 3	28
PL	Parasitic patches length	30
PW	Parasitic patches width	30

2.2. Antenna Design Discussion. Before the antenna design in this paper, the principle of uniformity of the electric field in the near field was first studied. Assuming that there is an equivalent model of a finite-length current source with a terminal connected load placed along the x-axis in space, the amplitude of the current source is distributed in a sinusoidal manner as shown in the following equation:

$$I(x) = I_0 \sin\left[\frac{2\pi}{\lambda}\left(\frac{L}{2} - x\right)\right], \left(-\frac{L}{2} \le x \le \frac{L}{2}\right). \quad (1)$$

Divide the current source into countless small current elements, and the radiation electric field at a certain point in space is the superposition of the small current source's radiation electric field at that point as shown in the following equation:

$$E(x, y, z) = \int_{-L/2}^{L/2} E_o[I(u), x, y, z)]\mathrm{d}u, \quad (2)$$

E_o is the electric field radiated by a small current element, and its three components in the spherical coordinate system are as follows:

$$E_{\text{or}} = \frac{\eta I_0 l \sin\theta}{2\pi r^2}\left[1 + \frac{1}{jkr}\right]e^{-jkr},$$

$$E_{o\theta} = j\frac{\eta I_0 l \cos\theta}{2\lambda r}\left[1 + \frac{1}{jkr} - \frac{1}{(kr)^2}\right]e^{-jkr}, \tag{3}$$

$$E_{o\varnothing} = 0.$$

Finally, utilizing the conversion formula between the rectangular coordinate system and the spherical coordinate system, the electric field value excited by the current source at an arbitrarily point in the rectangular coordinate system can be obtained. When there is in-phase current on the current element, the electric field value is maximum at the center above the current element, and the farther it deviates from the center position, the smaller the electric field value. This paper uses two single-branch microstrip lines with mutually perpendicular ends loaded to generate a uniform two-dimensional electric field in the near-field region. To ensure in-phase current on a single branch, the length of a single branch node satisfies the following inequality. Actual length can be obtained through simulation optimization.

$$\text{SPL1} \leq \frac{1}{2}\lambda_g. \tag{4}$$

The principle of a uniform electric field E_z perpendicular to the antenna surface is not the same as E_x and E_y. For the convenience of application, most of the reader/writer antennas are low-plane antennas, so it is not feasible to directly generate a vertical electric field using the vertical current. Assuming there is a planar magnetic ring above the antenna, the electric field perpendicular to the antenna surface can be obtained according to Maxwell's equation in (5). According to the Ampere theorem of (6), it can be analyzed that four centrally symmetric current sources with adjacent phase differences of 90° can generate a magnetic ring above them. Therefore, it is possible to utilize a centrally symmetric four-branch microstrip line to generate a uniform E_z. To make the current on the surface of each branch in phase, its length is designed to be about a quarter wavelength as shown in (7). Due to the introduction of parasitic patches, reverse currents appear on the surface of branches. To counteract this reverse current, each branch is designed as an arrow type.

$$\oint_l H \bullet \mathrm{d}l = \iint_S J \bullet \mathrm{d}S + \iint_S \frac{\partial D}{\partial t} \bullet \mathrm{d}S, \tag{5}$$

$$H = \frac{(2\pi \times I \times r)}{l}, \tag{6}$$

$$\text{SPL2} \approx \frac{1}{4}\lambda_g. \tag{7}$$

2.3. Principle of Three-Dimensional Uniformity of Electric Field. When unlike ports operate, the current distribution on the surface microstrip line is shown in Figure 2. From Figure 2(a), it can be seen that when Port 1 is working, the current on the four branches with central symmetry is reversed. According to Ampere's law, this current distribution will generate a magnetic field above the antenna as shown in Figure 3(a). It can be observed that the magnetic field in the horizontal plane above the antenna presents a circular shape, and there will be a uniform vertical electric field around the circular magnetic field as shown in Figure 4(a). This alternating electric field activates the chip inside the linearly polarized electrically coupled tag placed along the z-direction by generating an induced electromotive force, thereby completing the information exchange between the reader and the tag. From Figure 2(b), it can be seen that when Port 2 is operating, electromagnetic energy is mainly focused on the single branch microstrip line along the x-axis direction and the left branch in the four branch microstrip line, and the total current flows along the x-axis direction. At this point, the magnetic field vector and electric field vector distribution above the antenna are shown in Figure 3(b) and Figure 4(b), respectively. A uniform electric field along the x-axis can detect linearly polarized labels placed along the x-direction within a certain area. As above, Figure 2(c) shows that when Port 3 is operating, electromagnetic energy is mainly concentrated on the single branch microstrip line along the y-axis direction and the lower branch of the four branch microstrip line, and the total current flows along the y-axis direction. At this point, there is a magnetic field in the x-direction above the antenna as shown in Figure 3(c). A uniform electric field in the y-direction will be generated above the antenna as shown in Figure 4(c). Ensure that labels placed in the y-direction can be accurately detected. From the electric field vector map above the antenna, it can be seen that the distribution of the electric field vector is disorderly when very close to the antenna. It is possible to read the linear polarization labels placed in arbitrary orientations. As the distance increases, the direction of the electric field vector gradually becomes regular. At this time, only tags whose polarization direction is consistent with the direction of the electric field can be detected. From the above analysis, it can be seen that when the three ports operate in a time-sharing manner, a uniform three-dimensional electric field can be generated on the surface of the proposed antenna.

The four rectangular patches in the second layer of the antenna structure are used to enhance the electric field strength above the antenna and expand the uniform distribution range of the electric field. In addition, it can also generate resonance with the top-layer radiator, expanding the impedance bandwidth of the antenna. Figure 5 shows the current distribution on the surface of four parasitic patches when three ports are operating separately. When port 1 is working, there is a reverse current on a pair of centrally symmetrical patches, and the phase difference of

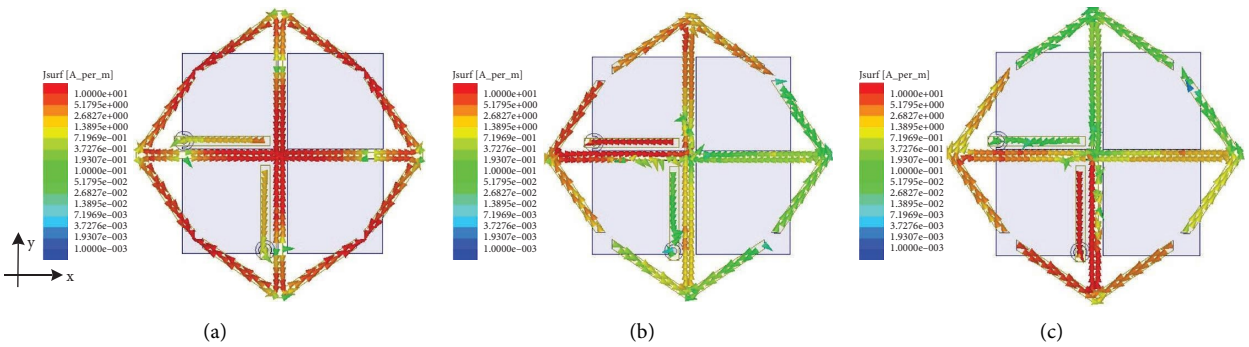

Figure 2: Current on the surface of the microstrip line when different ports operate. (a) Only Port 1 operates. (b) Only Port 2 operates. (c) Only Port 3 operates.

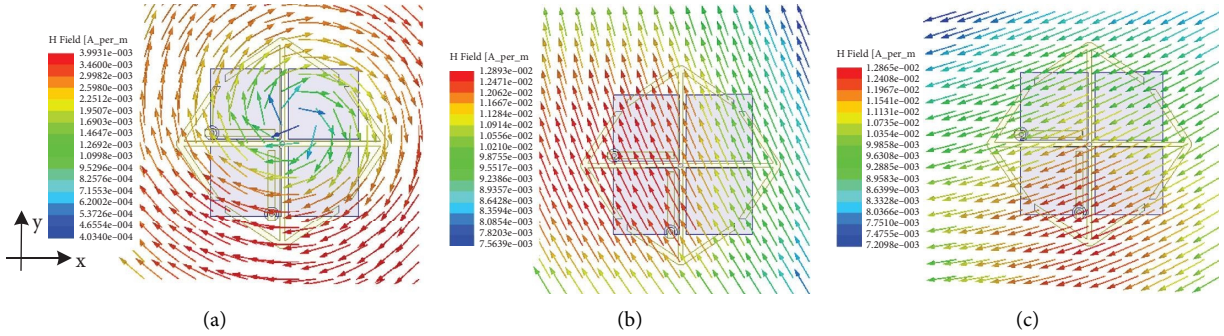

Figure 3: Distribution of magnetic field vectors in the horizontal plane $z = 100$ mm above the antenna when different ports work. (a) Only Port 1 operates. (b) Only Port 2 operates. (c) Only Port 3 operates.

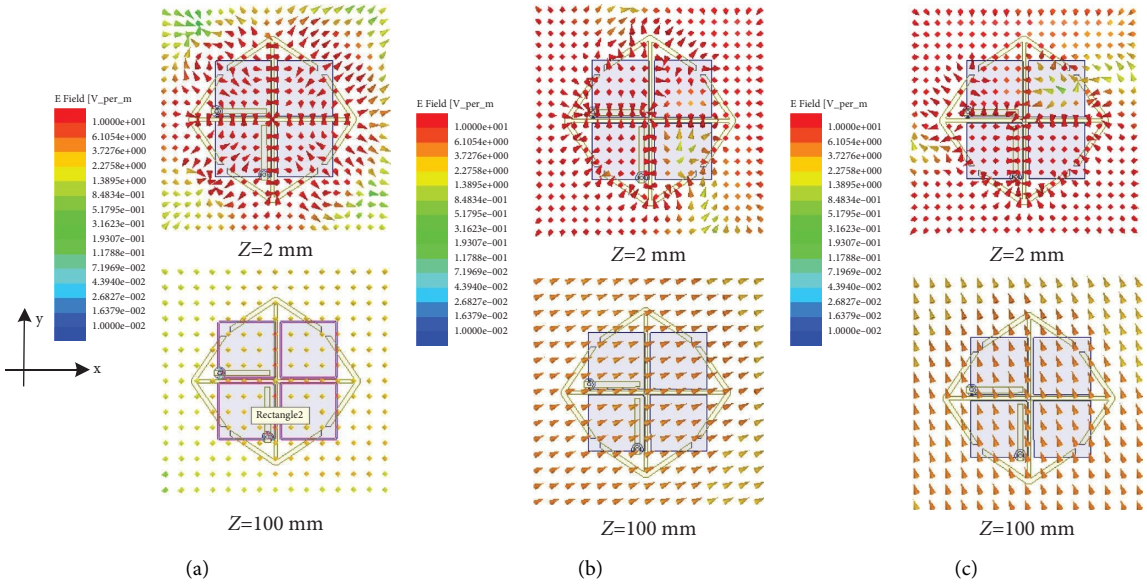

Figure 4: Distribution of electric field vectors in the horizontal plane $z = 2$ mm and $z = 100$ mm above the antenna when different ports work. (a) Only Port 1 operates. (b) Only Port 2 operates. (c) Only Port 3 operates.

the surface currents of adjacent patches approximately 90°, which is similar to the surface current of the four-branch microstrip line, and it has the same component as the surface current of the four-branch microstrip line. When Port 2 or Port 3 is operating, the current on the patches is mainly concentrated on the bottom left or top left patches. The induced current will also have an impact on the field distribution above the antenna. The electromagnetic energy in space mainly comes from the surface current of the radiation structure.

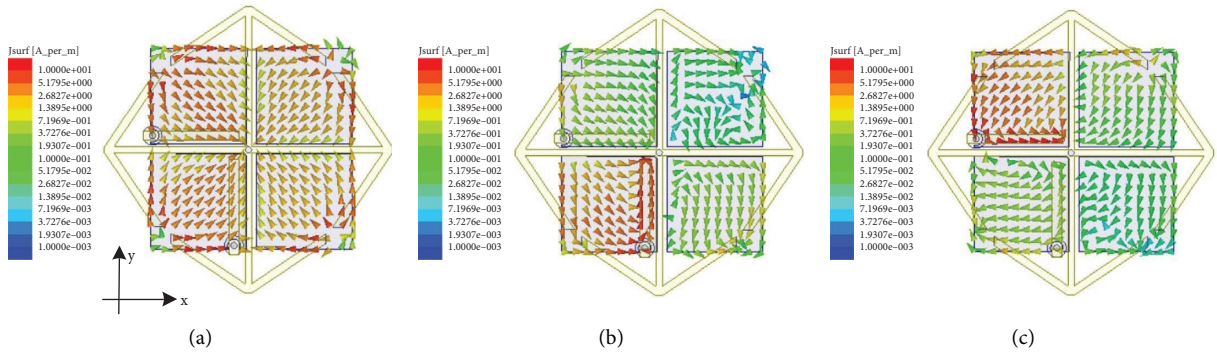

Figure 5: Induced current distribution on parasitic patches. (a) Only Port 1 operates. (b) Only Port 2 operates. (c) Only Port 3 operates.

3. Simulation Results and Discussion

3.1. Reflection Coefficient and Isolation. This paper uses HFSS to simulate the proposed antenna [21]. The simulation model of the antenna prototype in HFSS is shown in Figure 1. The simulation results of S_{11}, S_{22}, and S_{33} (reflection coefficient of each port) are shown in Figure 6. The reflection coefficients of the three ports are less than −10 dB in the bandwidth of 0.72 to 1.06 GHz, which meets the bandwidth standard of RFID and certain broadband requirements. The antenna proposed in this paper has good impedance matching in the UHF RFID band range (860–960 MHz). Figure 7 depicts the isolation degree between various ports S_{12}, S_{13}, and S_{23}. The port isolation of the antenna within the 860–960 MHz bandwidth is less than −31.6 dB, indicating very low interference between ports.

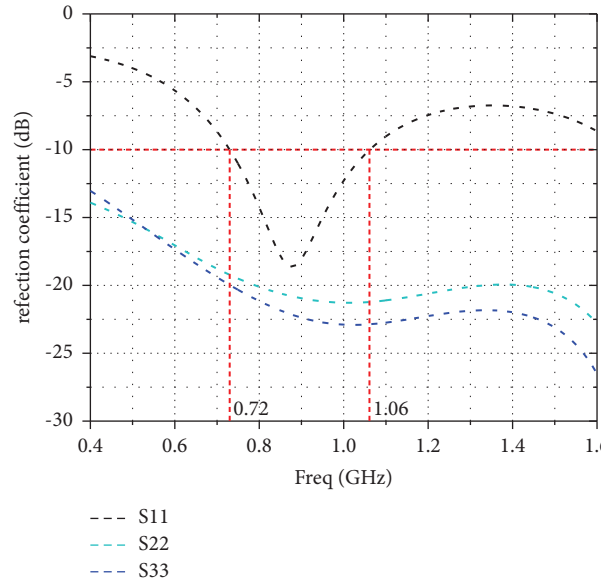

Figure 6: Reflection coefficient of different ports operating of the proposed antenna.

3.2. Parametric Study. Figures 8 and 9 plot the reflection coefficient and isolation of the proposed antenna at different substrate heights. Figure 8 is a graph of different substrate heights SH1. As SH1 increases, the impedance bandwidth of Port 1 widens, and the reflection coefficient S_{11} shifts downwards. When SH1 = 2 mm, the reflection coefficients S_{22} and S_{33} are significantly better than when SH1 is at other values, and the impedance bandwidth of Ports 2 and 3 is also the widest. When SH1 takes different values, the isolation will undergo irregular changes, but it is less than −25 db in the 860–960 MHz frequency band. The effect of the second layer substrate height SH2 on antenna performance is shown in Figure 9. With the SH2 changes, the port impedance bandwidth hardly changes, but there is a slight fluctuation in the value of the reflection coefficient. The impact of SH2 on isolation S_{12} and S_{13} in the 1–1.6 GHz frequency band is greater than that of low frequency. The isolation S_{23} decreases with the increase of SH2. Comparing Figures 8 and 9, it can be observed that the thickness of the first substrate SH1 has a greater impact on antenna performance than the thickness of the second substrate SH2.

The impact of the dimensions of the substrate on antenna performance is shown in Figures 10 and 11. Figure 10 is the study of the width W of the substrate. The change of W value has almost no effect on the impedance bandwidth. With the change of W, the reflection coefficient will slightly move up and down. The change in W value also has little impact on the isolation degrees S_{12} and S_{13} but has a certain impact on S_{23}. When W = 117 mm, isolation degrees S_{23} at low frequencies are significantly better than when W is other values. The influence of the change in length L of the substrate on the reflection coefficient and isolation of the proposed antenna is consistent with the influence of W as shown in Figure 11. Therefore, the size of the substrate has a sure impact on the isolation S_{23} at low frequencies.

3.3. Far-Field Three-Dimensional Direction Map. The far-field three-dimensional direction map of different ports operating the proposed antenna is presented in Figure 12. As can be seen that the maximum far-field gain is less than −27 dBi, indicating that the antenna has the characteristics of low gain in the far field, and it will avoid misreading tags in the far field area in actual application scenarios. Therefore, the antenna meets the performance requirements of the near-field reader-writer antenna.

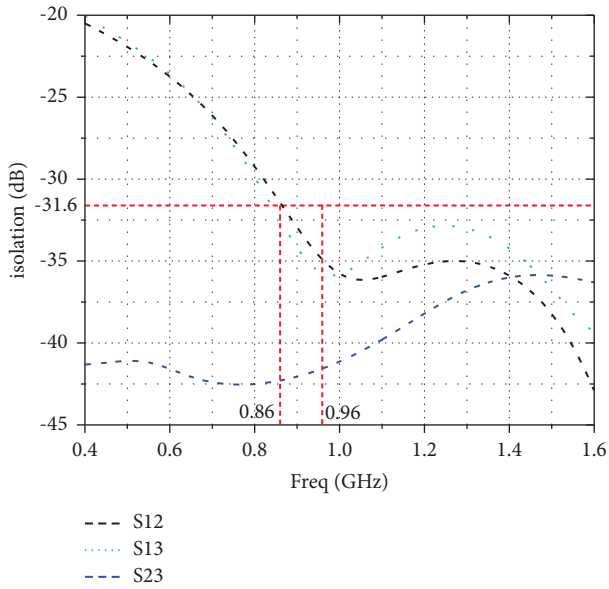

Figure 7: Isolation between adjacent ports of the proposed antenna.

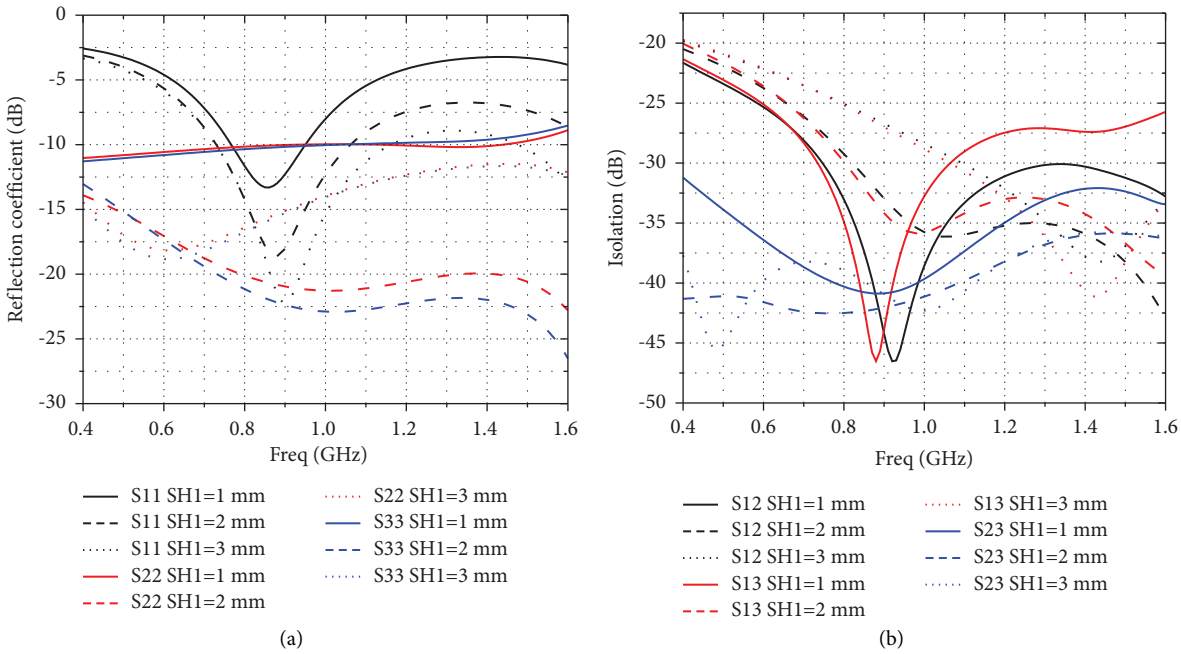

Figure 8: Reflection coefficient and isolation of different substrate heights SH1. (a) Reflection coefficient. (b) Isolation.

3.4. Electric Pattern. When only Port 1 is active, a plane parallel to the antenna surface and away from the proposed antenna above 2, 10, 50, and 100 mm, and the E_z distribution diagrams as shown in Figure 13(a). The E_z field is evenly distributed in a controlled area, and the reading range decreases as the distance increases. Figure 13(b) presents the E_x scalar distribution at the same height in the same plane when only Port 2 operates. The E_x field strength above the antenna is uniform and controllable. Figure 13(c) shows the E_y distribution when only Port 3 operates. Similarly, the controllable area above the antenna has a uniform E_y field strength.

Figure 14 illustrates the 3D distribution of the electric field at 2, 10, 50, and 100 mm for the antenna without parasitic patches. By comparing the uniform distribution range of the electric field in Figures 13 and 14, can be seen that the uniform distribution range of the field decreases after removing the parasitic patches.

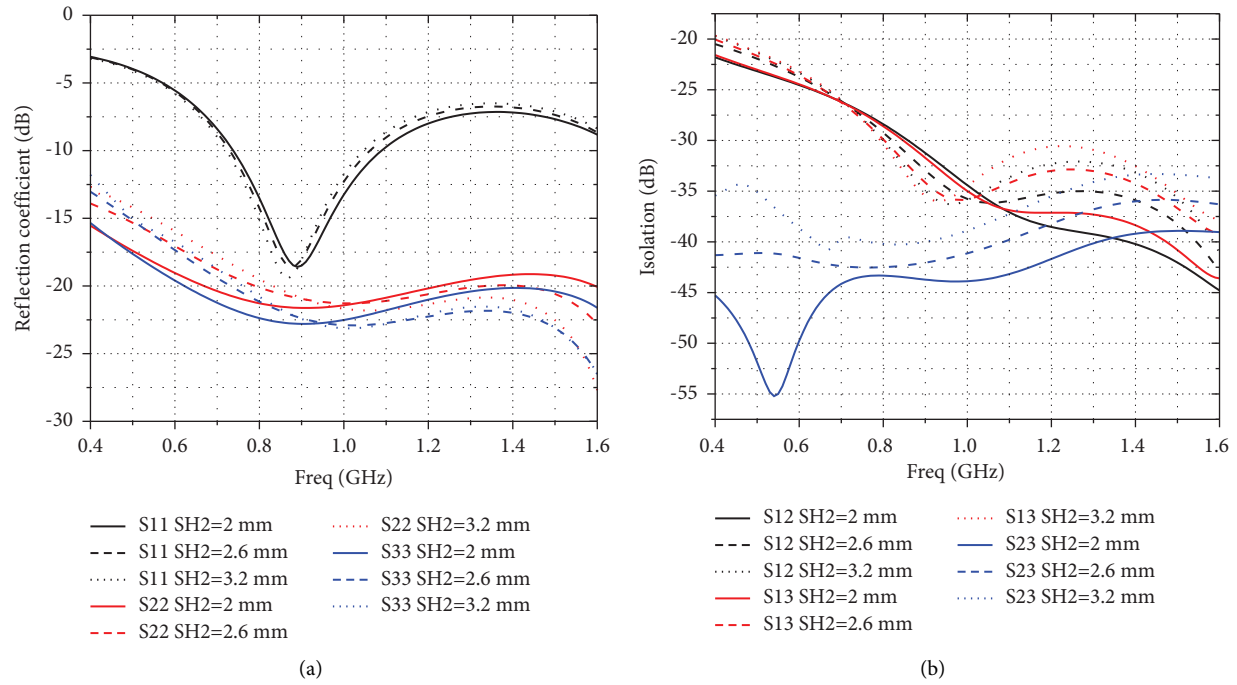

Figure 9: Reflection coefficient and isolation of different substrate heights SH2. (a) Reflection coefficient. (b) Isolation.

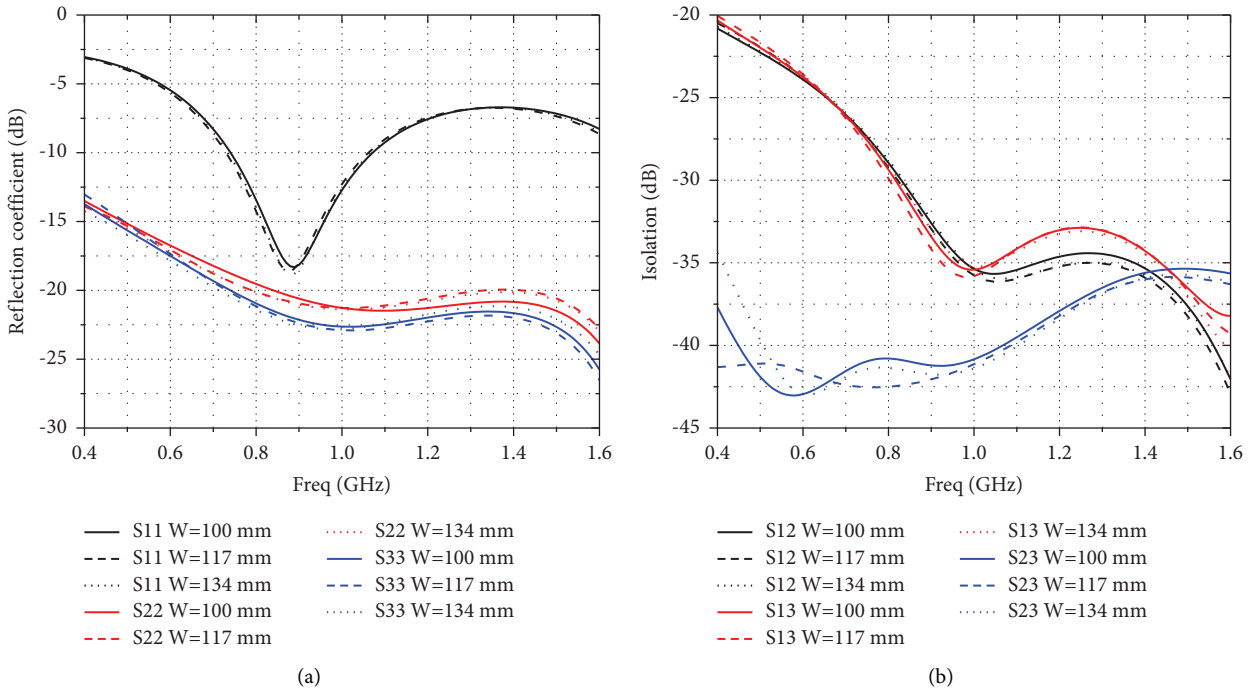

Figure 10: Reflection coefficient and isolation of different substrate heights *W*. (a) Reflection coefficient. (b) Isolation.

4. Measurement Results

To verify the correctness of the simulation results, the proposed antenna is processed, and its actual performance indicators are measured. Figure 15 shows the physical processing picture of the proposed antenna prototype. A 50 Ω SMA adapter is soldered at the feed port of the antenna, and a 50 Ω chip resistor of the 0805 packages is soldered at the end of the microstrip line.

In this paper, the impedance-matching bandwidth of the antenna is measured using the Agilent 8753ES vector network analyzer. Connect the adapter to the coaxial line of the vector network analyzer to measure each port reflectance coefficient of the proposed antenna. The comparison of the

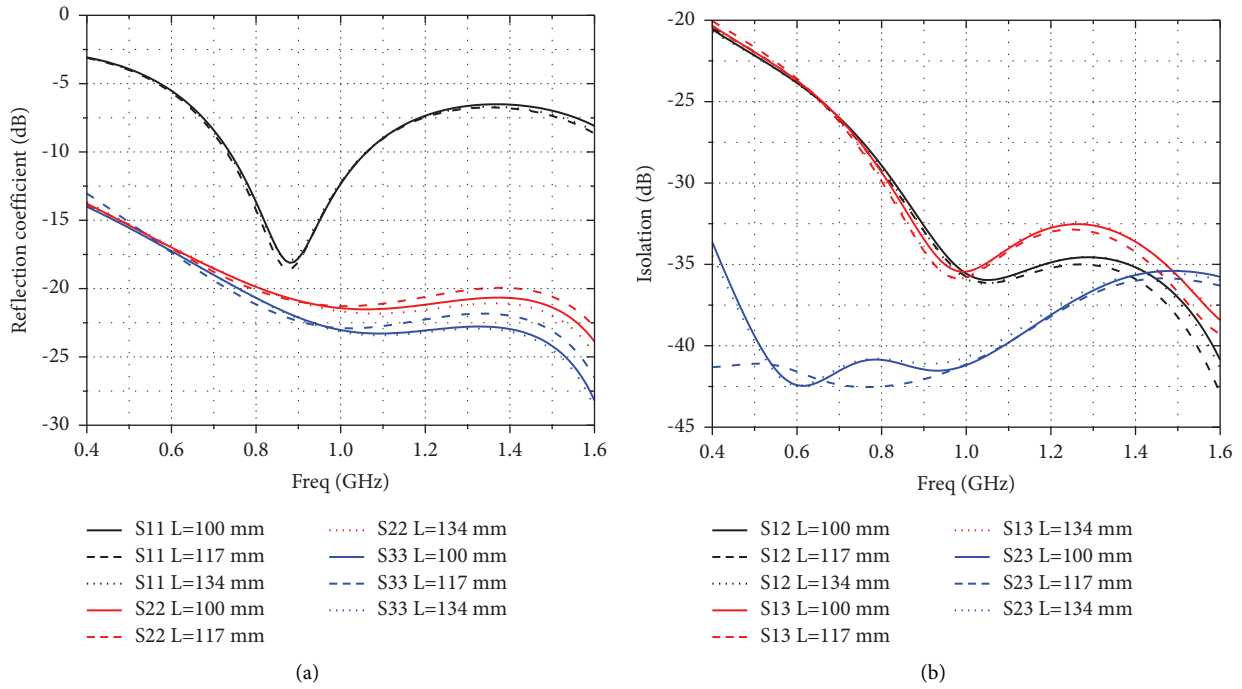

Figure 11: Reflection coefficient and isolation of different substrate heights L. (a) Reflection coefficient. (b) Isolation.

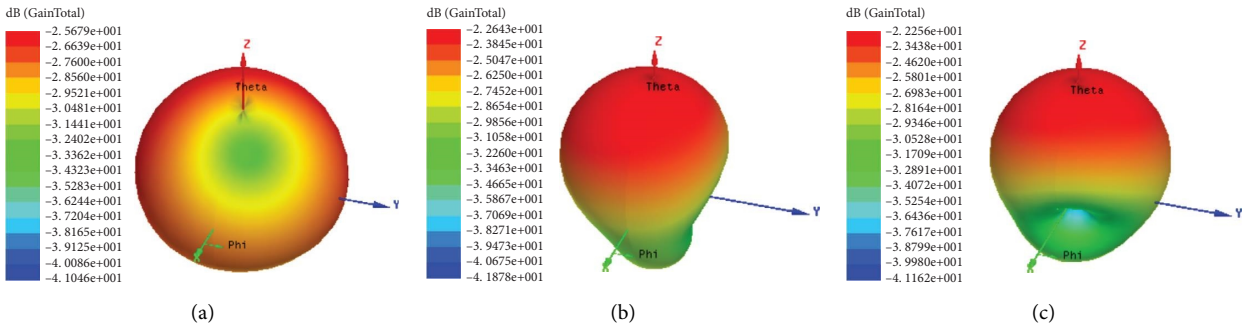

Figure 12: Far-field three-dimensional direction map of different ports operating the proposed antenna. (a) Only Port 1 operates. (b) Only Port 2 operates. (c) Only Port 3 operates.

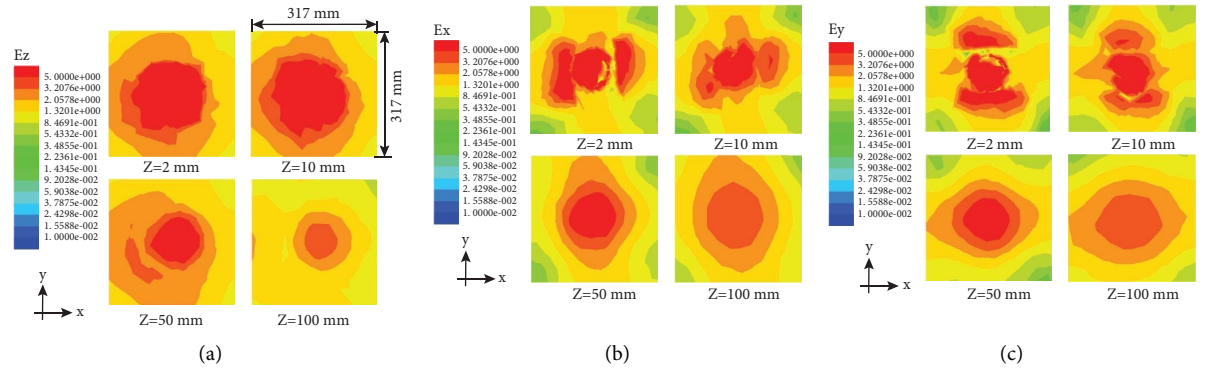

Figure 13: The plane parallel to the antenna surface away from the proposed antenna above 2, 10, 50, and 100 mm electric distribution map. (a) E_z distribution map. (b) E_x distribution map. (c) E_y distribution map.

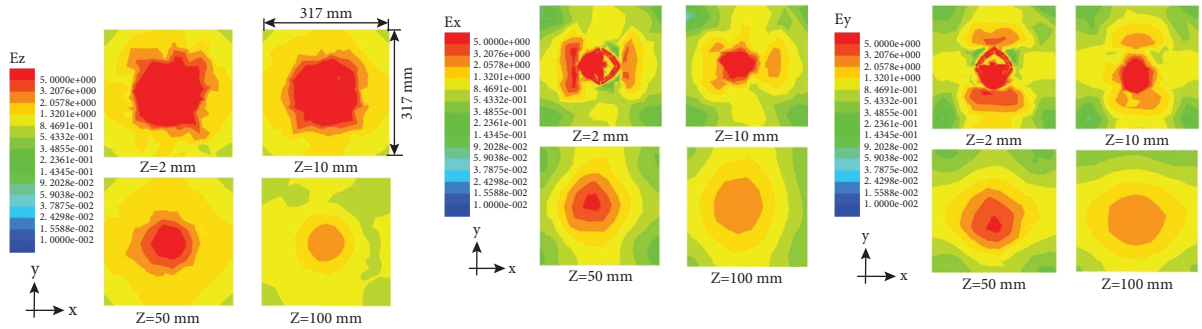

Figure 14: The plane parallel to the antenna surface away from the antenna without parasitic patches above 2, 10, 50, and 100 mm electric distribution map. (a) E_z distribution map. (b) E_x distribution map. (c) E_y distribution map.

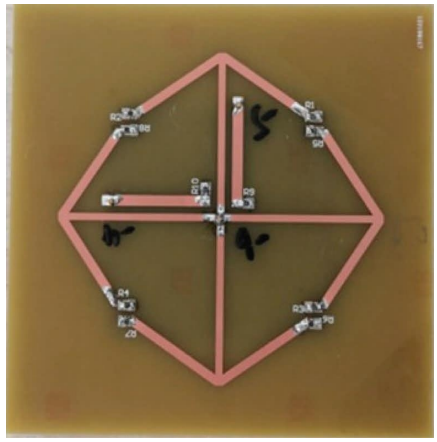

Figure 15: Processing physical picture of the proposed antenna.

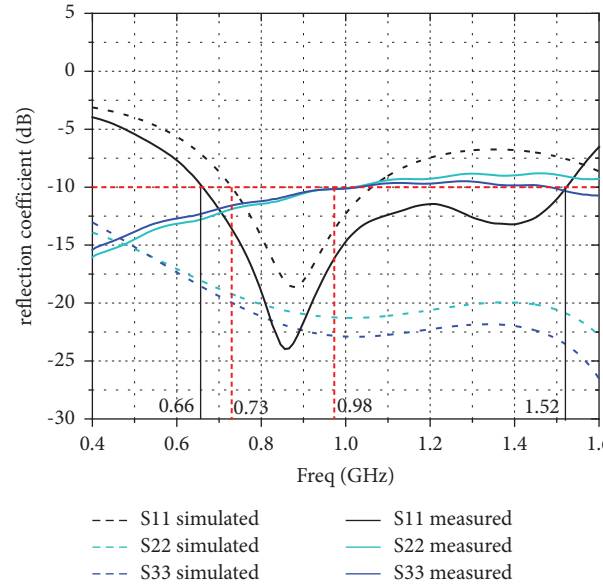

Figure 16: Simulated and measured results of the reflection coefficient of different ports operating of the proposed antenna.

simulation and measurement results of the reflection coefficients of each port of the antenna as shown in Figure 16. The measurement results display that the bandwidth with a reflection coefficient of less than −10 dB ranges from 0.66 to 0.98 GHz, including the UHF RFID (860–960 MHz) frequency range. Figure 17 represents the simulation and test results of the isolation degree between different ports. The test results show that the isolation degrees S_{12}, S_{13}, and S_{23} between ports are less than −24.6 dB in the 0.86 to 0.96 GHz frequency band. Compared to the simulation results, the slight deviation between the reflection coefficient and the isolation degree, which is caused by fabrication error.

The detection range of tags is one of the important performance indicators of the reader antenna. This paper uses two types of labels to detect the actual reading performance of the proposed antenna, respectively, Alien A9662 and Alien SIT.

Figure 18 shows the testing scenario of the label Alien A9662. The proposed antenna is connected to the Impinj Speedway R420 reader [22] with an output power of 30 dBm and a frequency of 920–925 MHz through a coaxial line. The reader is connected to the computer through a network cable to detect the reading range of labels placed in different directions. A foam board with a dimension of 226.5 mm × 189 mm is placed parallel to the antenna surface, its surface is equally divided into 15 grids, and a 17 mm × 70 mm Alien A9662 dipole tag is pasted to the center of each grid along the x-axis as shown in Figure 18(a). Move the foam plate along the z-axis to get the reading area of labels at diverse heights, repeat the test 10 times, record the label reading range at each height, and calculate the average read rate. The reading range of the tags placed along the y-axis can be tested by rotating the foam board in Figure 18(a) by 90°. Paste the label vertically on a foam board with a dimension of 165 mm × 165 mm and divided it into 25 grids. Similarly, move the foam board along the z-axis direction to measure the reading volume of the label pile along the z-axis direction as shown in Figure 18(c). Figure 19 depicts the detection results of tags placed along the x, y, and z directions. From the figure, it can be seen that when tags are placed along the x-axis, the reading volume with a 100% reading rate is 226.5 mm × 113.4 mm × 40 mm. When tags are placed along the y-axis, the reading volume is 226.5 mm × 113.4 mm × 20 mm. When labels are

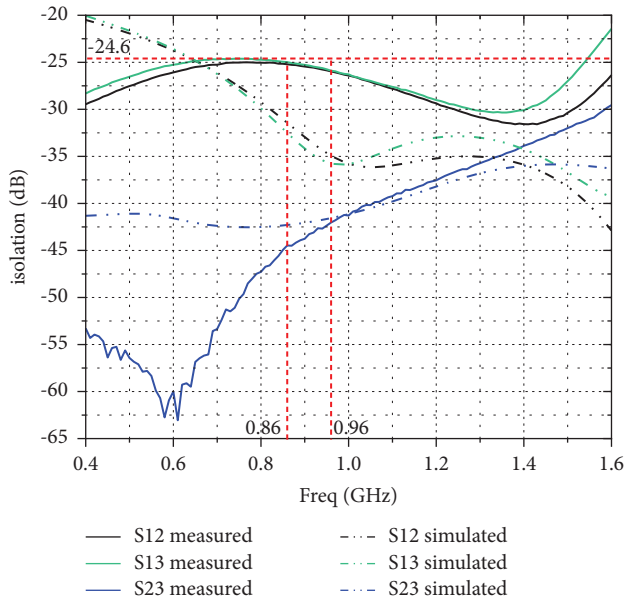

Figure 17: Simulated and measured results of the isolation between distinct ports of the proposed antenna.

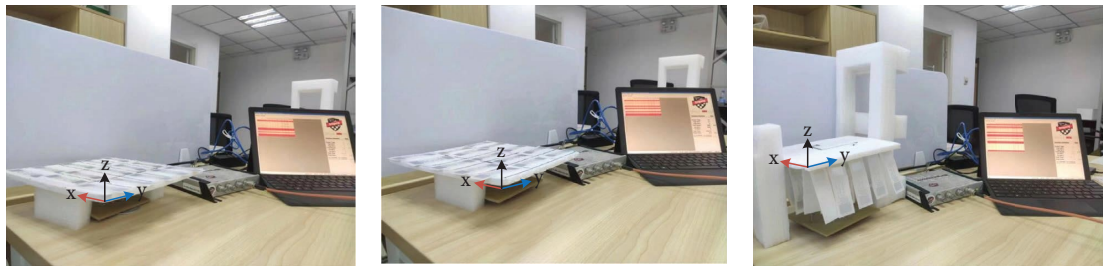

(a) (b) (c)

Figure 18: The testing scenario of the tag Alien A9662. (a) Tags are placed along the x-axis. (b) Tags are placed along the y-axis. (c) Tags are placed along the z-axis.

placed along the z-axis, the reading volume is 99 mm × 99 mm × 70 mm. Therefore, the reading volume of the label with a 100% reading rate in the three-dimensional direction is 99 mm × 99 mm × 20 mm. The testing scenario of the tag Alien A9662 placed on books is shown in Figure 20. Figure 21 shows the detection results of the reading range of the tag placed on the book. At this time, the reading volume with a 100% reading rate in the three-dimensional direction of the tag is 99 mm × 99 mm × 20 mm. Compared with Figure 19, it is found that when the Alien A9662 tags are placed on a book-like medium, there is a slight deviation in the tag detection results, but it has little impact on the reading range.

Figure 22 gives the detection scenario of the Alien SIT tag. The tags are pasted on the foam plate parallel to the antenna surface along the x, y, and z directions, respectively. The dimensions of the foam plate above the antenna are 80 mm × 80 mm, and its surface is divided into 16 grids. When testing the reading range of labels in different directions, a 12 mm × 9 mm Alien SIT near-field label in the corresponding direction is pasted at the center of each grid. Figure 23 plots the detection results of placing the tags directly above the antenna. It can be seen that when the tags are placed along the x-direction, the reading volume with a 100% reading rate of the label is 40 mm × 40 mm × 20 mm. When the tags are placed along the y-direction, the reading volume with a 100% reading rate of the label is 40 mm × 40 mm × 15 mm. When the tags are placed along the z-direction, the reading volume with a 100% reading rate of the label is 40 mm × 40 mm × 5 mm.

The reading volume of the proposed antenna with a 100% reading rate in the three-dimensional direction of the Alien SIT near-field antenna is 40 mm × 40 mm × 5 mm. The testing scenario of the tag Alien SIT placed on books as shown in Figure 24. Figure 25 shows the measurement results of the foam board with a near-field label placed on the book, and the size of the foam board is consistent with Figure 22. It can be found that books have little impact on the reading range of tags in the x- and y-axis directions, but they have a certain impact on the reading of tags in the z-axis direction.

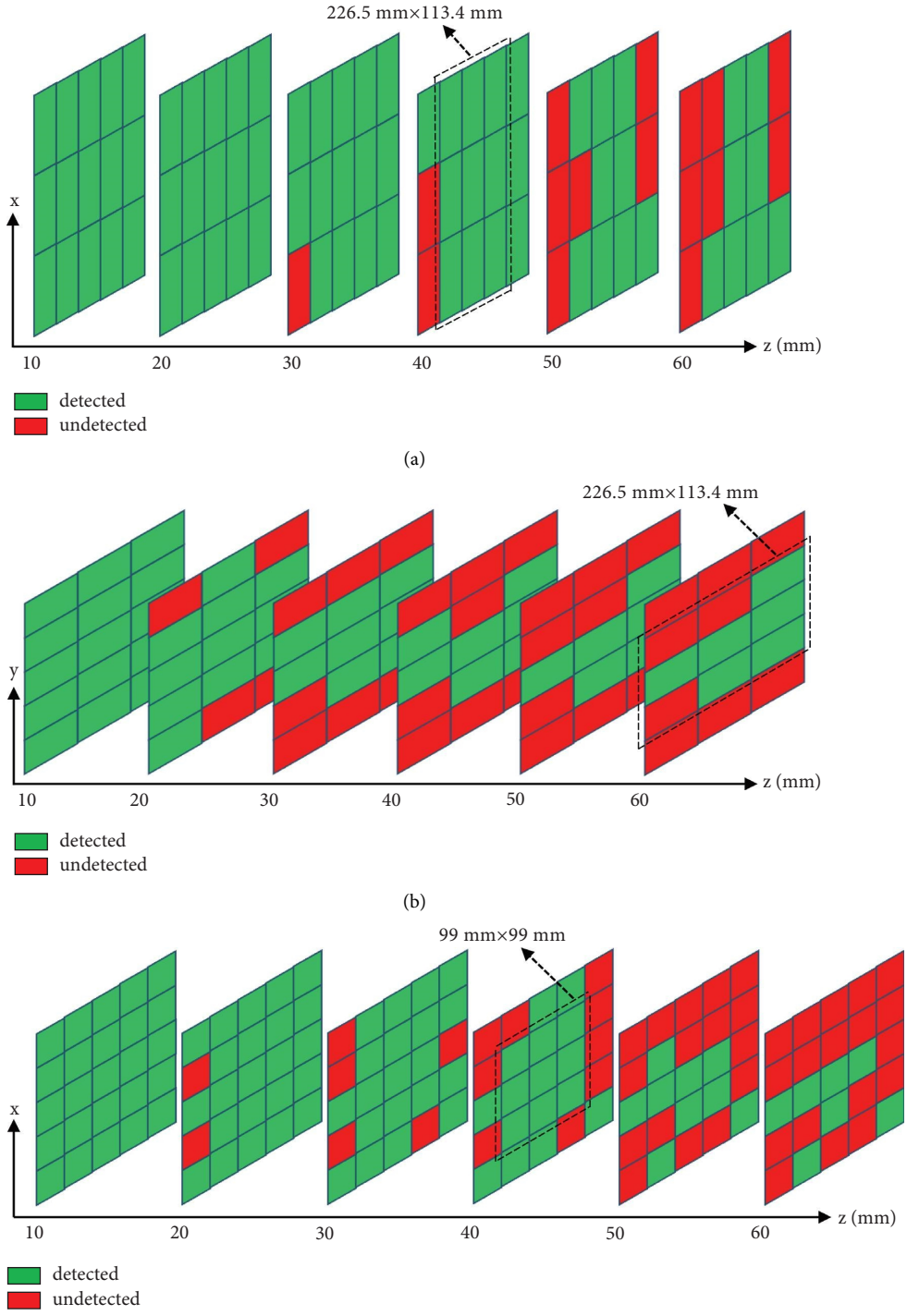

Figure 19: The detection results of the Alien A9662 tags placed along the x, y, and z directions. (a) Tags are placed along the x-axis. (b) Tags are placed along the y-axis. (c) Tags are placed along the z-axis.

(a) (b) (c)

Figure 20: The testing scenario of the tag Alien A9662 placed on books. (a) Tags are placed along the x-axis. (b) Tags are placed along the y-axis. (c) Tags are placed along the z-axis.

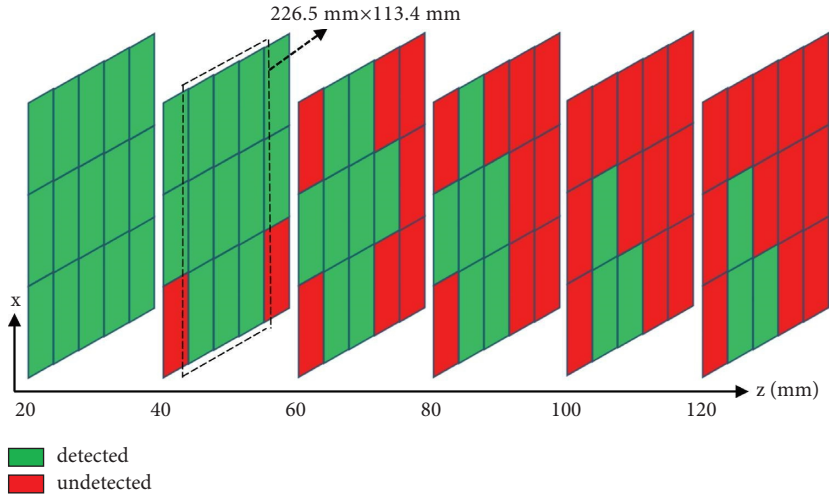

(a)

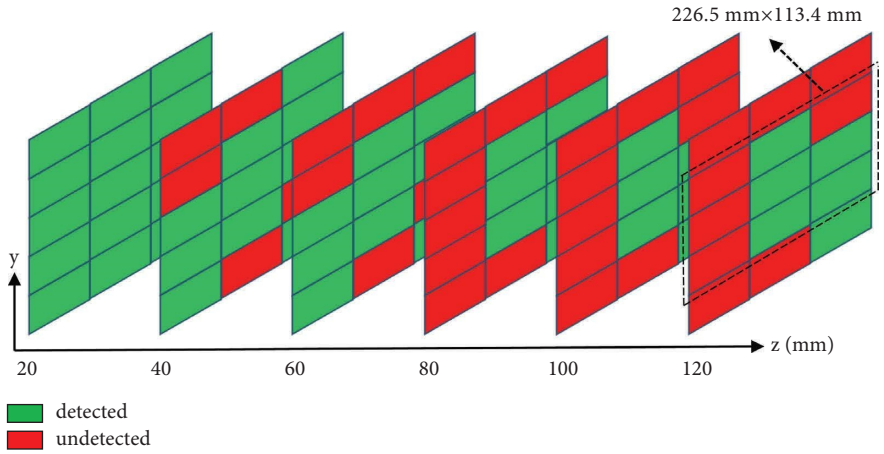

(b)

Figure 21: Continued.

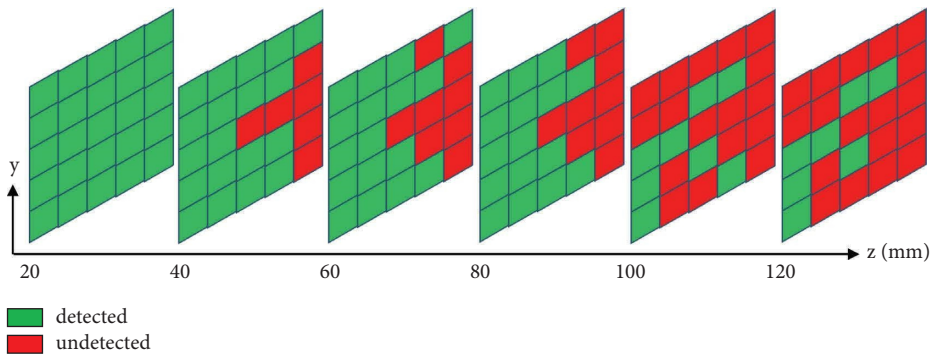

(c)

Figure 21: The detection results of the Alien A9662 tags placed on books. (a) Tags are placed along the x-axis. (b) Tags are placed along the y-axis. (c) Tags are placed along the z-axis.

(a) (b) (c)

Figure 22: The testing scenario of the tag Alien SIT. (a) Tags are placed along the x-axis. (b) Tags are placed along the y-axis. (c) Tags are placed along the z-axis.

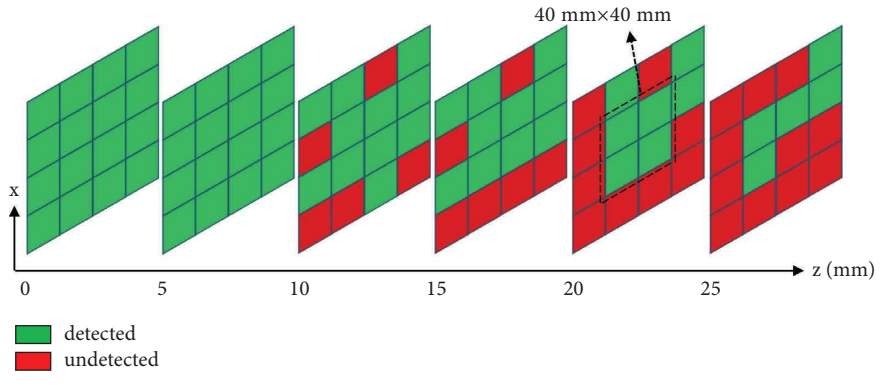

(a)

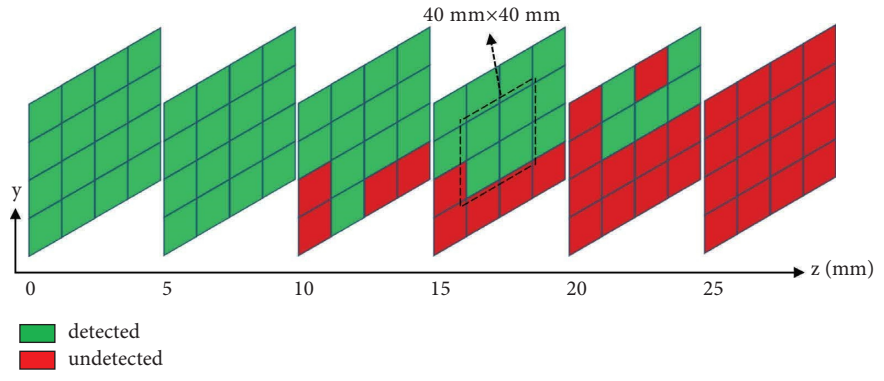

(b)

Figure 23: Continued.

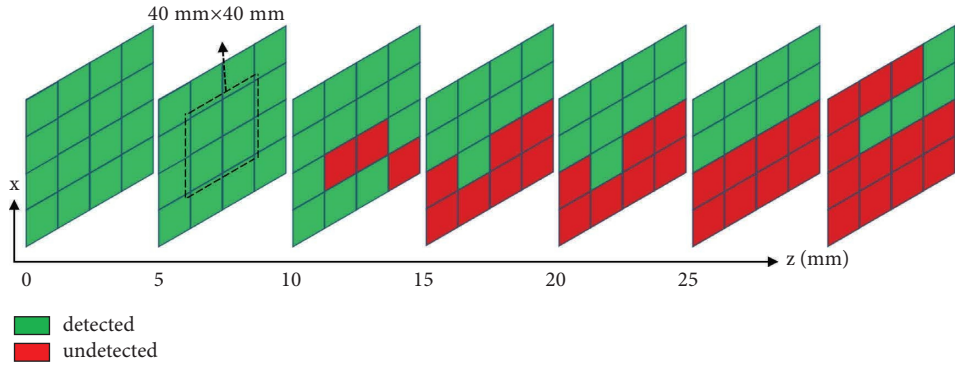

(c)

Figure 23: The detection results of the Alien SIT tags placed along the x, y, and z directions. (a) Labels are placed along the x-axis. (b) Labels are placed along the y-axis. (c) Labels are placed along the z-axis.

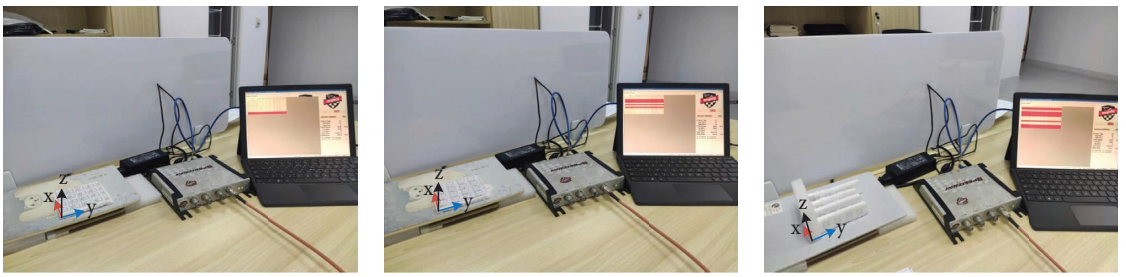

(a) (b) (c)

Figure 24: The testing scenario of the tag Alien SIT placed on books. (a) Tags are placed along the x-axis. (b) Tags are placed along the y-axis. (c) Tags are placed along the z-axis.

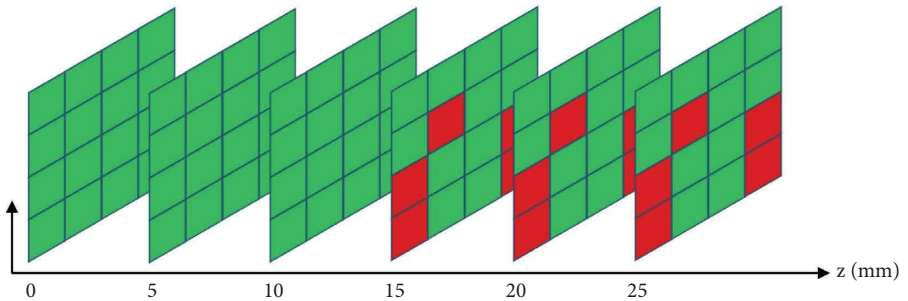

(a)

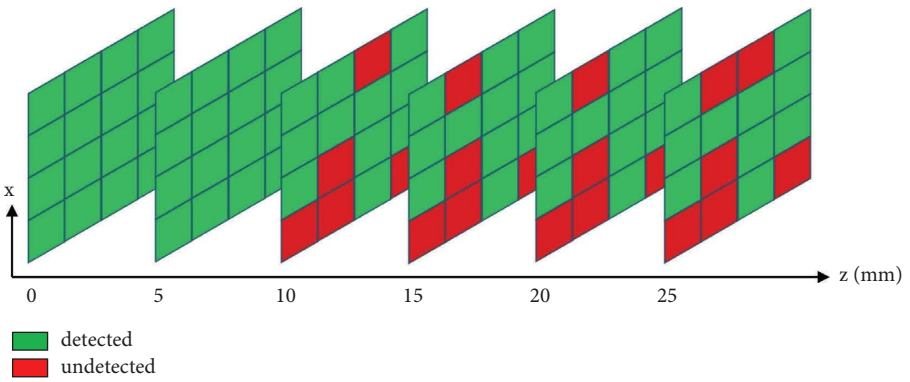

(b)

Figure 25: Continued.

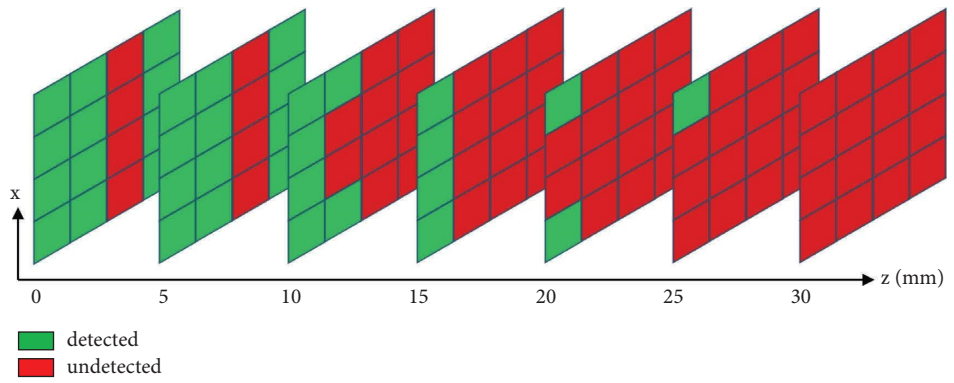

(c)

Figure 25: The detection results of the Alien SIT tags placed on books. (a) Tags are placed along the x-axis. (b) Tags are placed along the y-axis. (c) Tags are placed along the z-axis.

Table 2: Comparison between the proposed and previous works.

References	Frequency range (GHz)	Far-field gain (dBi)	Antenna size (mm^2)	Field uniform dimension	Using tag types	Read range (mm^3)
[15]	0.82–0.96	−10	225.6 ∗ 220	Two	Alien A9662	450 ∗ 450 ∗ 350
[16]	0.92–0.925	−6	270 ∗ 150	Two	Alien A9662	400 ∗ 320 ∗ 300
[17]	0.8–0.94	—	250 ∗ 250	Two	LAB-ID Inlay UH100	640 ∗ 6640 ∗ 100
This work	0.66–0.98	−27	117 ∗ 117	Three	Alien A9662	99 ∗ 99 ∗ 20

Table 2 shows a comparison between the manufactured antennas and other previous works. It can be seen that the antenna proposed in this paper has the lowest far-field gain, which can greatly reduce the misreading rate in practical applications. The proposed antenna is smaller in size compared to other antennas. Although the reading volume for the same tag is smaller, it can read tags in an arbitrarily direction. The size of the antennas in paper [15,17] is not much different, and both can normally detect tags parallel to the antenna surface. However, for different types of tags, the reading volume varies greatly.

5. Conclusion

This paper proposes a reconfigurable microstrip antenna to achieve a uniform electric field in the three-dimensional direction and presents its configuration, principle, characteristics, simulation, and measurement results of the antenna. The simulation results show that the uniformity of the electric field in the three-dimensional direction of the antenna is quite good. The measurement results illustrate that the reading area of the tag above the antenna is concentrated, and the tags in the far field cannot be detected, which verifies the theory's correctness.

Data Availability

The data used to support the findings of this study are included in the article.

Conflicts of Interest

The authors declare that they have no conflicts of interest.

Acknowledgments

This work was supported by the Fundamental Research Funds for the Central Universities.

References

[1] R. Want, "An introduction to RFID technology," *IEEE Pervasive Computing*, vol. 5, no. 1, pp. 25–33, 2006.

[2] D. P. Chechi, "The RFID technology and its applications: a review," *International Journal of Electronics, Communication & Instrumentation Engineering Research and Development*, vol. 2, no. 3, pp. 109–120, 2012.

[3] Y. Duroc and S. Tedjini, "Rfid: a key technology for Humanity," *Comptes Rendus Physique*, vol. 19, no. 1-2, pp. 64–71, 2018.

[4] P. V. Nikitin, K. V. S. Rao, and S. Lazar, "An overview of near field UHF RFID," in *Proceedings of the 2007 IEEE International Conference on RFID*, pp. 167–174, Grapevine, TX, USA, March 2007.

[5] K. Jaakkola and P. Koivu, "Low-cost and low-profile near field UHF RFID transponder for tagging batteries and other metal objects," *IEEE Transactions on Antennas and Propagation*, vol. 63, no. 2, pp. 692–702, 2015.

[6] T. A. Morgado, J. M. Alves, J. S. Marcos et al., "Spatially confined UHF RFID detection with a metamaterial grid," *IEEE Transactions on Antennas and Propagation*, vol. 62, no. 1, pp. 378–384, 2014.

[7] M. Kaur, M. Sandhu, N. Mohan, and P. S. Sandhu, "RFID technology principles, advantages, limitations & its applications," *International Journal of Computer and Electrical Engineering*, vol. 3, no. 1, pp. 151–157, 2011.

[8] F. Fuschini, C. Piersanti, L. Sydanheimo, L. Ukkonen, and G. Falciasecca, "Electromagnetic analyses of near field UHF

RFID systems," *IEEE Transactions on Antennas and Propagation*, vol. 58, no. 5, pp. 1759–1770, 2010.

[9] A. Michel and P. Nepa, "UHF-RFID desktop reader antennas: performance analysis in the near-field region," *IEEE Antennas and Wireless Propagation Letters*, vol. 15, pp. 1430–1433, 2016.

[10] J. Shi, X. Qing, Z. Chen, and C. K. Goh, "Electrically large dual-loop antenna for UHF near-field RFID reader," *IEEE Transactions on Antennas and Propagation*, vol. 61, no. 3, pp. 1019–1025, 2013.

[11] J. Shi, X. Qing, and Z. N. Chen, "Electrically large zero-phase-shift line grid-array UHF near-field RFID reader antenna," *IEEE Transactions on Antennas and Propagation*, vol. 62, no. 4, pp. 2201–2208, 2014.

[12] Y. Yao, C. Cui, J. Yu, and X. Chen, "A meander line UHF RFID reader antenna for near-field applications," *IEEE Transactions on Antennas and Propagation*, vol. 65, no. 1, pp. 82–91, 2017.

[13] J. Ouyang, Y. Yan, L. Zhuang, and J. Guo, "A novel meander line RFID reader antenna or UHF near-field applications," in *Proceedings of the 2018 IEEE International Symposium on Antennas and Propagation & USNC/URSI National Radio Science Meeting*, pp. 1297-1298, Boston, MA, USA, July 2018.

[14] A. S. Andrenko and M. Kai, "Novel design of UHF RFID near-field antenna for smart shelf applications," in *Proceedings of the 2013 Asia-Pacific Microwave Conference Proceedings (APMC)*, pp. 242–244, Seoul, Republic of Korea, November 2013.

[15] Y. Yao, Y. Liang, J. Yu, and X. Chen, "Design of a multi-polarized RFID reader antenna for UHF near-field applications," *IEEE Transactions on Antennas and Propagation*, vol. 65, no. 7, pp. 3344–3351, 2017.

[16] Y. Yao, X. Ren, Y. Liang, J. Yu, and X. Chen, "Multipolarized reader antenna with periodic units based on electric field coupling for UHF RFID near-field applications," *IEEE Transactions on Antennas and Propagation*, vol. 67, no. 8, pp. 5265–5271, 2019.

[17] X. Ren, Y. Yao, Y. Liang, J. Yu, and X. Chen, "A novel multi-polarization UHF RFID reader antenna for near-field applications," in *Proceedings of the 2020 IEEE International Symposium on Antennas and Propagation and North American Radio Science Meeting*, pp. 1599-1600, Montreal, Canada, July 2020.

[18] A. Michel, M. Rodriguez Pino, and P. Nepa, "Reconfigurable modular antenna for NF UHF RFID smart point readers," *IEEE Transactions on Antennas and Propagation*, vol. 65, no. 2, pp. 498–506, 2017.

[19] A. Birwal, V. Kaushal, and K. Patel, "Investigation of circularly polarized CPW fed antenna as a 2.45 GHz RFID reader," *IEEE Journal of Radio Frequency Identification*, vol. 6, pp. 593–600, 2022.

[20] F. Xue, Y. Zhang, J. Li, and H. Liu, "Circularly polarized cross-dipole antenna for UHF RFID readers applicated in the warehouse environment," *IEEE Access*, vol. 11, pp. 38657–38664, 2023.

[21] Z. Cendes, "The development of HFSS," in *Proceedings of the USNC-URSI Radio Science Meeting*, pp. 39-40, Fajardo, PR, USA, July 2016.

[22] Impinj, "Speedway RFID reader documentation," 2016, https://support.impinj.com/hc/en-us/articles/202755298-Speedway-Reader-Documents-Downloads.